Earth and Planetary Science Letters 527 (2019) 115796

Contents lists available at ScienceDirect

Earth and Planetary Science Letters

www.elsevier.com/locate/epsl

Sharpness of the hemispherical boundary in the inner core beneath the northern Pacific

Ryohei Iritani *, Hitoshi Kawakatsu, Nozomu Takeuchi

Earthquake Research Institute, The University of Tokyo, 1-1-1 Yayoi, Bunkyo-ku, Tokyo, 113-0032, Japan

ARTICLE INFO

Article history:
Received 30 March 2019
Received in revised form 23 August 2019
Accepted 27 August 2019
Available online xxxx
Editor: M. Ishii

Keywords:
inner core
waveform inversion
differential travel time
hemispherical boundary
sharpness

ABSTRACT

The hemispherical nature of heterogeneities of the isotropic velocity and attenuation of the inner core has been extensively studied by seismic observations, but consensus on the character of the boundary between two hemispheres has not yet been achieved. To investigate the hemispherical boundary in detail, we analyze core phase data whose ray paths propagate beneath the northern Pacific. We employ a waveform inversion approach based on simulated annealing to measure the differential traveltime and the attenuation parameter of the core phases. Measured differential traveltimes for data from European stations for events in the Fiji-Tonga region show positive anomalies consistent with the eastern hemisphere model, while those from USArray for events in Indonesia show relatively small values. Ray-theory based forward modeling of the differential traveltimes is conducted by varying the shape and the transition width of the boundary. An arc-like shape boundary that connects points (0°N, 159°W) on the equator and (79°N, 110°E) in far north with a transition width of ∼600 km best explains the observed differential traveltimes rather than a sharp boundary. This model also accounts for the observed variation of attenuation parameters.

1. Introduction

The existence of the hemispherical heterogeneity in the topmost of the Earth's inner core, fast velocity and high attenuation in the eastern hemisphere and slow velocity and low attenuation in the western hemisphere, has been widely recognized by many seismological studies (e.g. Tanaka and Hamaguchi, 1997; Wen and Niu, 2002; Cao and Romanowicz, 2004; Yu and Wen, 2006). While this characteristic feature would be a piece of clarification for the dynamics of the inner core, full understanding of the hemispherical structures is not yet achieved. With expanding seismic networks, however, the coverage of the sampling region of seismic data is dramatically extended. Hence, more complex heterogeneities of the inner core have been increasingly revealed by recent studies in terms of the lateral regional variation of the velocity and attenuation structure (e.g. Tanaka, 2012; Cormier and Attanayake, 2013; Iritani et al., 2014a; Attanayake et al., 2014; Pejić et al., 2019) and frequency dependence of attenuation (Iritani et al., 2014b), and also in terms of the lateral variation of anisotropy (Irving and Deuss, 2015).

In addition to the depth profiling of the velocity and attenuation structure, delineating the transition structure over two hemispheres, i.e. the hemispherical boundary, may provide another important clue for constraining the inner core dynamics. Tanaka and Hamaguchi (1997), who first reported the presence of the hemispherical structure, proposed a spherical harmonic expansion of the hemispherical boundary by measurements of the differential traveltime of PKIKP and PKPbc (Fig. 1a) that are sensitive to the top 350 km of the inner core. In latter studies based on global data analysis of the same phases, however, the reported hemispherical boundaries (assumed to be on meridians) have inconsistencies in terms of their locations in the range from 14°E to 60°E beneath Africa and from 160°E to 151°W beneath Pacific (e.g. Garcia and Souriau, 2000; Garcia, 2002; Irving and Deuss, 2011). As for regional studies for the northern Pacific utilizing PKIKP and PKPbc, Miller et al. (2013) proposed a boundary at a longitude of 173°E ± 4° in latitudes greater than 60°N for the top ∼200 km of the inner core, and Yu et al. (2017) at a longitude of 160°W. Note that, in these studies, only the position of the boundary is estimated, and the nature of the velocity transition between two hemispheres is not investigated.

For the study of the top 100 km of the inner core employing PKIKP and PKiKP (a core phase reflected at the inner core boundary (ICB)), Waszek et al. (2011) and Waszek and Deuss (2011) analyzed global datasets to propose sharp (i.e. step-like) hemispherical boundaries on meridians at longitudes of 173°W and 10°E. They also reported that both boundaries shifted eastward with depth.

* Corresponding author.
E-mail address: ryohei.iritani@gmail.com (R. Iritani).

https://doi.org/10.1016/j.epsl.2019.115796
0012-821X/

On the other hand, Ibourichene and Romanowicz (2018) recently reported a western-hemisphere-like feature of the differential traveltime anomalies in the North polar region that belongs to the eastern hemisphere for some of the models with boundaries on meridians that leaves some inconsistencies among observations even for the shallower depth range.

As for the explanation for the hemispherical heterogeneities, several geodynamical models have been proposed. One class of models indicate that a differential growth rate of the inner core driven by thermal heterogeneities at the lowermost mantle results in lateral heterogeneities at ICB (Sumita and Olson, 1999; Aubert et al., 2008; Gubbins et al., 2011). According to this class of models, the fastest growth occurs beneath Southeast Asia, corresponding to the eastern hemisphere. Another class of models proposes that a grain growth due to translational convection of the inner core material from a solidifying side (the western hemisphere) to a melting side (the eastern hemisphere) (Monnereau et al., 2010; Alboussière et al., 2010). Geballe et al. (2013) suggested, by conducting numerical simulations, that the translational model might be able to explain the sharp hemispherical boundary as observed in Waszek et al. (2011). Translational convection in the inner core, however, could occur under very limited viscosity conditions (Deguen, 2012; Mizzon and Monnereau, 2013; Deguen et al., 2013). Moreover, more buoyancy to drive convection in the core is expected in the opposite hemispheres for these models. Further observational evidence to constrain the inner core's physical state and growth process is required to understand the dynamics of the inner and outer core.

Here, we investigate a transition structure of hemispherical heterogeneity of the inner core beneath the northern Pacific. We apply an array-based waveform inversion (Iritani et al., 2010; Iritani et al., 2014a) to core phase data that propagate the target region to investigate the location and shape of the hemispherical boundary as well as its sharpness.

2. Data

We analyze the vertical component of broadband core phase data. Core phases are categorized by traveling regions in the Earth's core, PKIKP that travels in the inner core and PKP that travels only in the outer core. PKP phases are also distinguished as PKPab and PKPbc depending on the associated traveltime curve branches (Fig. 1a). The data set used in this study consists of two directional event-station pairs, seismograms observed by permanent European stations (hereafter referred to as EUArray) for events in the Fiji-Tonga region and USArray for events near Indonesia. We select event data containing PKIKP and PKP (i.e. the epicentral distance between 145–155 degree) with Mw greater than 5.7 in the term of 2009–2018. We discard low S/N ratio data and resultant waveforms consist of 2,108 and 1,172 traces for EUArray and USArray, respectively. These seismograms are collected from the Data Management Center of IRIS. The distribution of events and stations and corresponding ray paths are shown in Fig. 1b. The sampling area of the inner core is from middle Asia to Pacific in the northern hemisphere. The propagation angles from the Earth's rotation axis for all event-station pairs are larger than 40 degrees and can be considered as equatorial paths that are not affected by anisotropy of the inner core. Each waveform is filtered by a second order zero-phase Butterworth band-pass filter between 0.5–1.5 Hz and therefore has a dominant frequency of 1 Hz.

3. Observations

3.1. Traveltime measurement

We employ a nonlinear waveform inversion based on simulated annealing (SA) (cf. Garcia et al., 2004; Iritani et al., 2010; Iritani et al., 2014a). This method optimizes model parameters to explain observed array data using the SA algorism (cf. Sen and Stoffa, 1995) and allows analyzing waveforms that contain several target phases that share a common input wavelet. As the detail of this method is described in Iritani et al. (2010) and Iritani et al. (2014a), we mention only the essence of the method here.

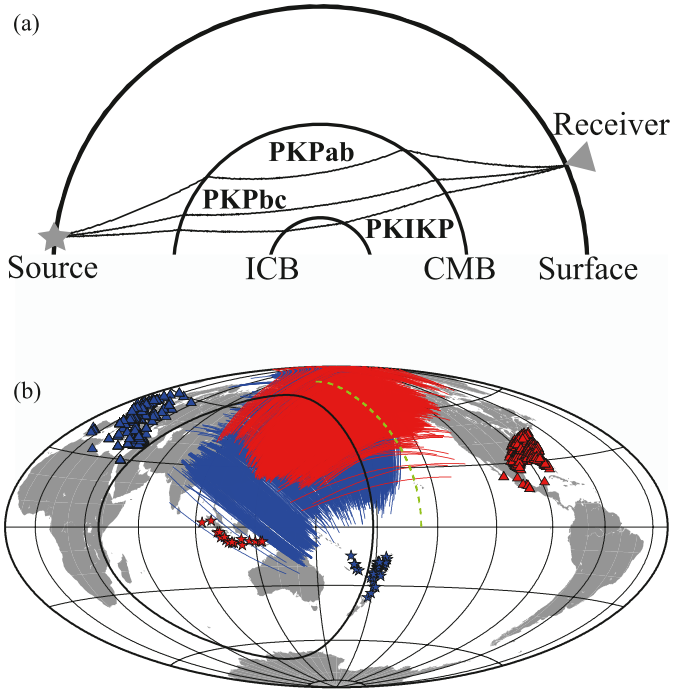

Fig. 1. (a) Ray paths of core phases, PKIKP, PKPbc and PKPab. (b) PKIKP ray paths in the inner core used in this study (bold lines). Stars and triangles represent the location of events and stations. Blue and red colors denote the data observed by stations in Europe and the US, respectively. The black solid line and green dashed line denote the hemispherical boundaries proposed by Tanaka and Hamaguchi (1997) and by this study, respectively. (For interpretation of the colors in the figure(s), the reader is referred to the web version of this article.)

As this method is applied for each event-array pair data set, three core phases in each seismogram can be parameterized by a common incident waveform among whole array data set, and parameters of amplitude and traveltime for each phase. Additionally, an attenuation operator is convolved in the modeling of PKIKP to take into account the attenuation effect of the inner core. After initializing all parameters, the process to minimize the residual between observed and modeled waveforms computed with perturbed parameters is executed according to the SA algorithm. In initializing traveltime parameters, we use theoretical traveltimes of three phases computed for the reference velocity model, AK135 (Kennett et al., 1995).

For the measurement of traveltime, as the ray paths of PKIKP and PKPbc are similar in the crust and mantle, the difference between PKIKP and PKP is conventionally considered as due to the heterogeneity in the inner core (Fig. 1a). In this study, traveltimes of PKIKP (t_{PKIKP}) and PKPbc (t_{PKPbc}) are used for the calculation of the differential traveltime between PKIKP and PKPbc, $dt = t_{\mathrm{PKPbc}} - t_{\mathrm{PKIKP}}$. Then, the residual between observations (dt_{obs}) and theoretical differential traveltimes computed for the AK135 model (dt_{cal}) is defined as the differential traveltime anomaly, $\Delta t_{\mathrm{obs}} = dt_{\mathrm{obs}} - dt_{\mathrm{cal}}$. Examples of the waveform inversion for EUArray and USArray are presented in Fig. 2. Model waveforms well explain observed data even for a distance range where three core phases overlap each other (145–147°) and observed traveltimes suggest faster arrivals of PKIKP phase in EUArray than those in USArray. The measured differential traveltime anomalies and at-

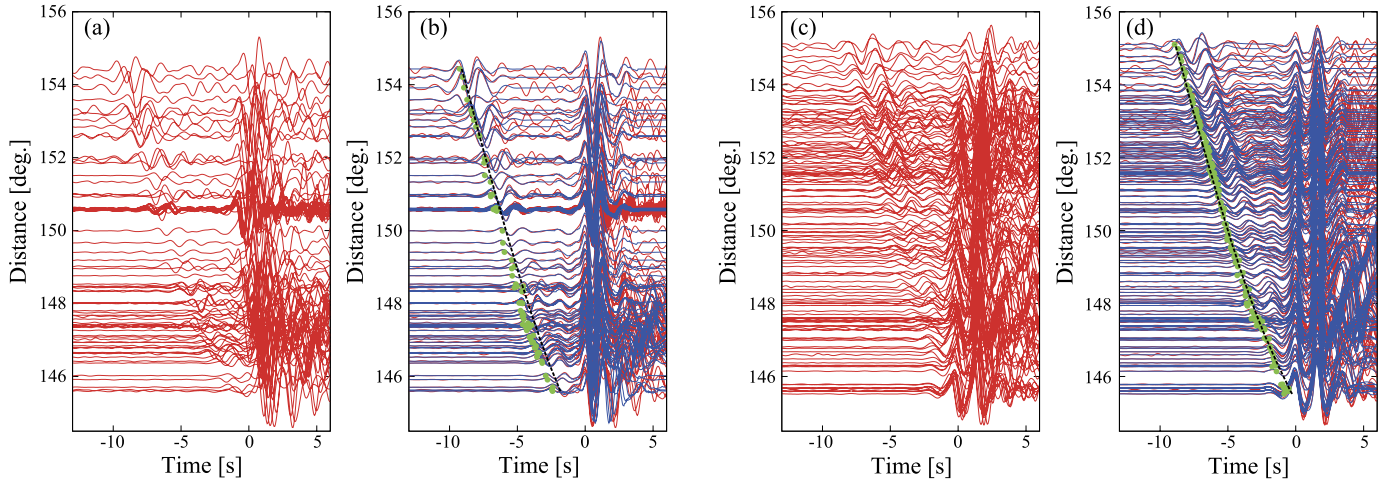

Fig. 2. Examples of the waveform inversion analysis. (a) A record section observed by EUArray for a M_W 6.4 earthquake in Fiji (4 May 2014). Seismograms are aligned with the theoretical traveltime of PKPbc. (b) Comparison between observed (red) and model waveforms (blue). Black dashed line and green dots denote theoretical and observed traveltimes of PKIKP. (c) The same as (a) for USArray data (a M_W 6.2 earthquake in Indonesia on 25 Jan. 2014). (d) The same as (b) for USArray data. Although PKPab phases are employed in the actual waveform analysis, we mainly show PKIKP and PKPbc here for the presentation purpose.

tenuation parameters are shown in Figs. 3a–3d for EUArray and USArray data. EUArray data indicate positive traveltime anomalies that are consistent with the eastern hemisphere velocity model of Iritani et al. (2014a) (Fig. 3e), while USArray data show relatively small (or no) anomalies (Fig. 3c). These observations suggest that the data of EUArray mainly samples the eastern hemisphere and those of USArray are affected by both hemispheres. On the other hand, attenuation parameters for both arrays in Fig. 3d show a similar feature suggesting high attenuation consistent with the model values computed with the attenuation model for the eastern hemisphere of Iritani et al. (2014a) (Fig. 3f).

Fig. 4 represents the distribution of differential traveltime anomalies at the turning points of PKIKP ray paths for EUArray and USArray: Figs. 4a and 4b are map-views and Figs. 4c–4e and Fig. 4f–4h are cross-sections projected onto a great-circle plane denoted by green lines, O–O' and P–P', in Figs. 4a and 4b. The cross-sections on O–O', which is nearly orthogonal to the reported hemispherical boundary, show different features for two array data in a range 60–80 angular distance from the western edge of the plane (O in Figs. 4a and 4c): large positive anomalies gradually become smaller toward the eastern side for EUArray data (Fig. 4c), while positive and negative anomalies are mixed for USArray data (Fig. 4d, e). On the other hand, the cross-sections on P–P', which is sub-parallel to the boundary, do not show systematic distribution of differential traveltime anomalies (Figs. 4f–4h). This indicates that traveltime anomalies of two-array datasets are affected differently by two hemispheres that help constraining the nature of the hemispherical transition in the studied area.

3.2. Delineating the hemispherical boundary

To explain the observed differential traveltime anomalies, we conduct ray theory based forward modeling of traveltime by varying the position of the hemispherical boundary and its shape as follows. We define a coordinate on the Earth's surface with considering the ellipticity of the Earth by setting the origin of the coordinate at the longitude of 110°E on the equator (O in Fig. 5) and considering two variable points on the equator and the northern part of the meridian at 110°E (Z and Y in Fig. 5). Then, for a given azimuth θ measured from the equator, we put $X(\theta)$ at an intersection point of a meridian at Z and a line along the minimal length path with θ from O. Finally, the new hemispherical boundary is defined by the trajectory of a point on the same minimal length path, $X'(\theta)$, defined as to have the distance between $X(\theta)$ and $X'(\theta)$, $XX'(\theta)$ by

$$XX'(\theta) = YN\left(\frac{ZX(\theta)}{ZN}\right)^2, \tag{1}$$

where N is the North Pole, and YN, ZN and $ZX(\theta)$ are distances from Y to N, Z to N and Z to $X(\theta)$, respectively. With this definition, $XX'(\theta)$, becomes 0 when $\theta = 0°$ and YN when $\theta = 90°$. The boundary becomes a meridian at a longitude of Z when Y locates at a latitude of 90° (the North Pole) and otherwise becomes an arc-like-shape. Once a boundary is defined with given a longitude of Z and a latitude of Y, theoretical differential traveltime anomalies (Δt_{cal}) can be computed based on the ray theory as the following,

$$\Delta t_{cal} = \int_{east} \delta s_{east} dl + \int_{west} \delta s_{west} dl \tag{2}$$

where $\delta s_{east(west)}$ is the slowness perturbation relative to AK135 in the eastern (western) hemisphere and dl is the length of an infinitesimal segment along the ray path. Note that 1-D velocity models estimated in Iritani et al. (2014a) are used for computation of the slowness perturbation in both hemispheres. Then, we calculate a root-mean-square (RMS) of residuals between theoretical traveltime anomalies and observed ones for all data as,

$$RMS = \sqrt{\frac{1}{N}\sum_{i=1}^{N}(\Delta t_{obs} - \Delta t_{cal})_i^2} \tag{3}$$

where i is an index of an event-station pair and N is the total number of data.

We conduct a grid search to find an optimal boundary in the range of 170°E–150°W for the longitude of Z and 70°N–90°N for the latitude of Y with a 1° interval. Fig. 6 shows the distribution of RMS residuals in the studied range. The minimum RMS value is obtained at the longitude of 159°W for Z and the latitude of 79°N for Y. We estimate error bars using the bootstrap technique (cf. Efron and Tibshirani, 1993) by randomly resampling traveltime anomalies among all observation allowing overlaps. We apply the same grid search process for each of 1,000 resampled data sets, and standard deviations of the optimal longitudes of Z and Y as ±3.2° and ±1.9°, respectively. The data set of EUArray is about

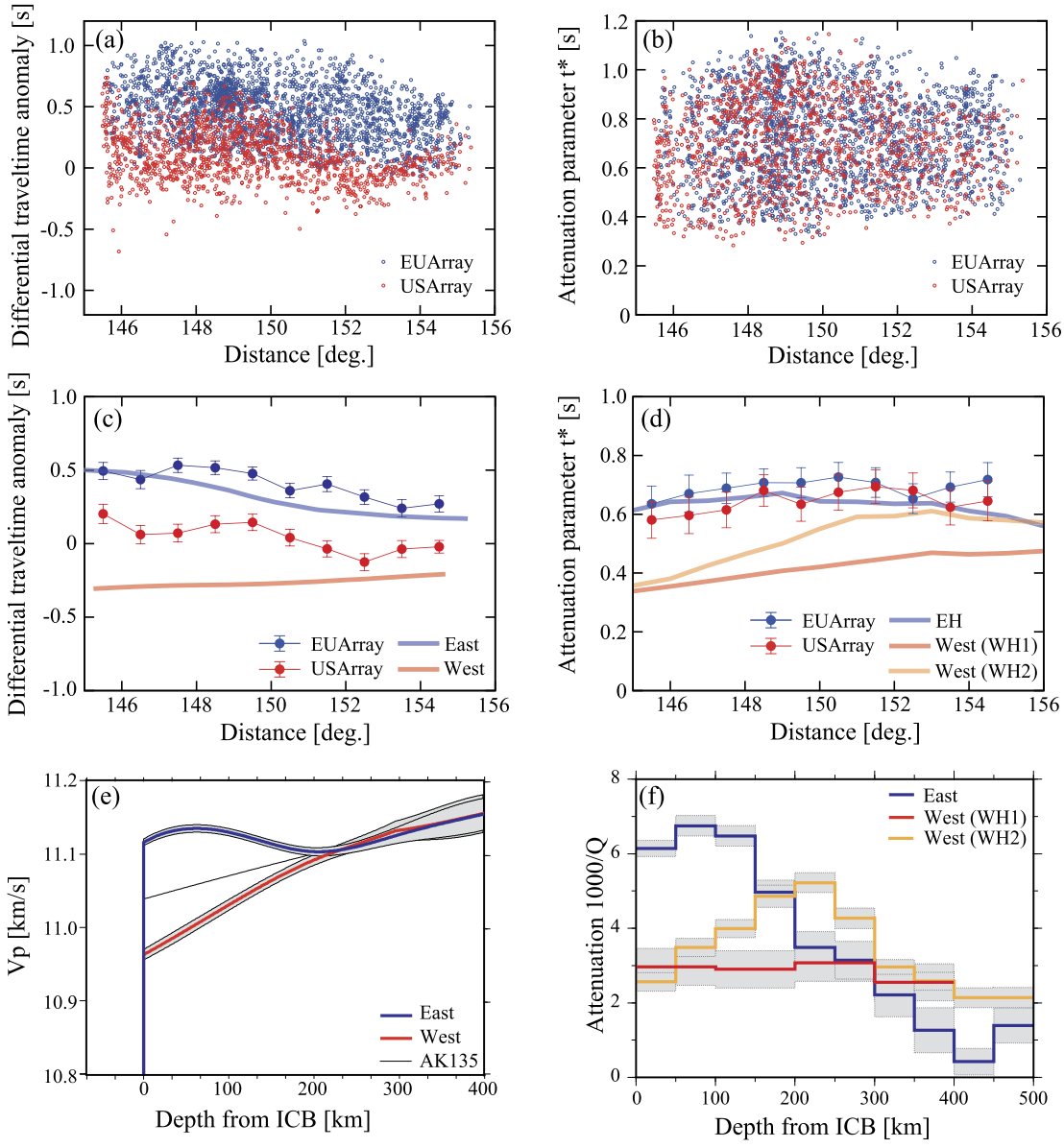

Fig. 3. (a) Observed differential traveltime anomalies referenced to AK135 and (b) attenuation parameters for EUArray (blue) and USArray data (red) as a function of the epicentral distance. (c) Averaged differential traveltime anomalies and (d) attenuation parameters for a distance bin of 1°. Thick lines in (c) and (d) represent model values computed for (e) velocity models and (f) attenuation models of the inner core studied in Iritani et al. (2014a).

twice larger than that of USArray. To evaluate a possible bias in the result due to the different amounts of two datasets, we conduct the same analysis for randomly reduced EUArray data that have the same number of seismograms with USArray data. We tested with 10 such reduced EUArray data and the original USArray data, and obtained the same result as that of the whole datasets, confirming the robustness of the result. Moreover, to evaluate the consistency of two array data, we perform the same analysis for each dataset separately; the resultant optimal hemispherical boundaries with single-array data are within the error bars from that with the whole datasets, which indicates that individual array data do constrain the boundary location and are consistent with each other.

3.3. Sharpness of the hemispherical boundary

To investigate the transitional nature of the hemispherical boundary, we further conduct a grid search by varying the width of the hemispherical velocity transition. As a structure of the transition, a linear variation of the velocity from the eastern hemisphere to the western hemisphere is assumed. First, we fix the hemispherical boundary as the optimal boundary, the arc-like boundary extending from 79°N, 110°E to 0°N, 159°W, obtained in Section 3.2 (hereafter referred to as the best (sharp) boundary). Then, we define a width of velocity variation as an angular distance at the ICB, and velocity structures are linearly connected between two hemispheres within a given width at each depth of the inner core (Fig. 7a). In the grid search process, we vary the width from 0 to 50-degree angular distances with a 2-degree interval. Note that the corresponding distance for 2 degrees at the ICB is about 42 km, and the boundary becomes a velocity jump (sharp boundary) from the eastern to the western structure for the case of a 0-degree wide transition. Next, we compute differential traveltimes using equation (2) considering a linear variation of the velocity structure for a given transition width to estimate the RMS residual denoted in equation (3). In computing RMS residuals, we count for only ray paths that are affected by the transitional variation for the largest width in the investigated range, i.e. only ray paths that sample the region within ±50 degrees from the best

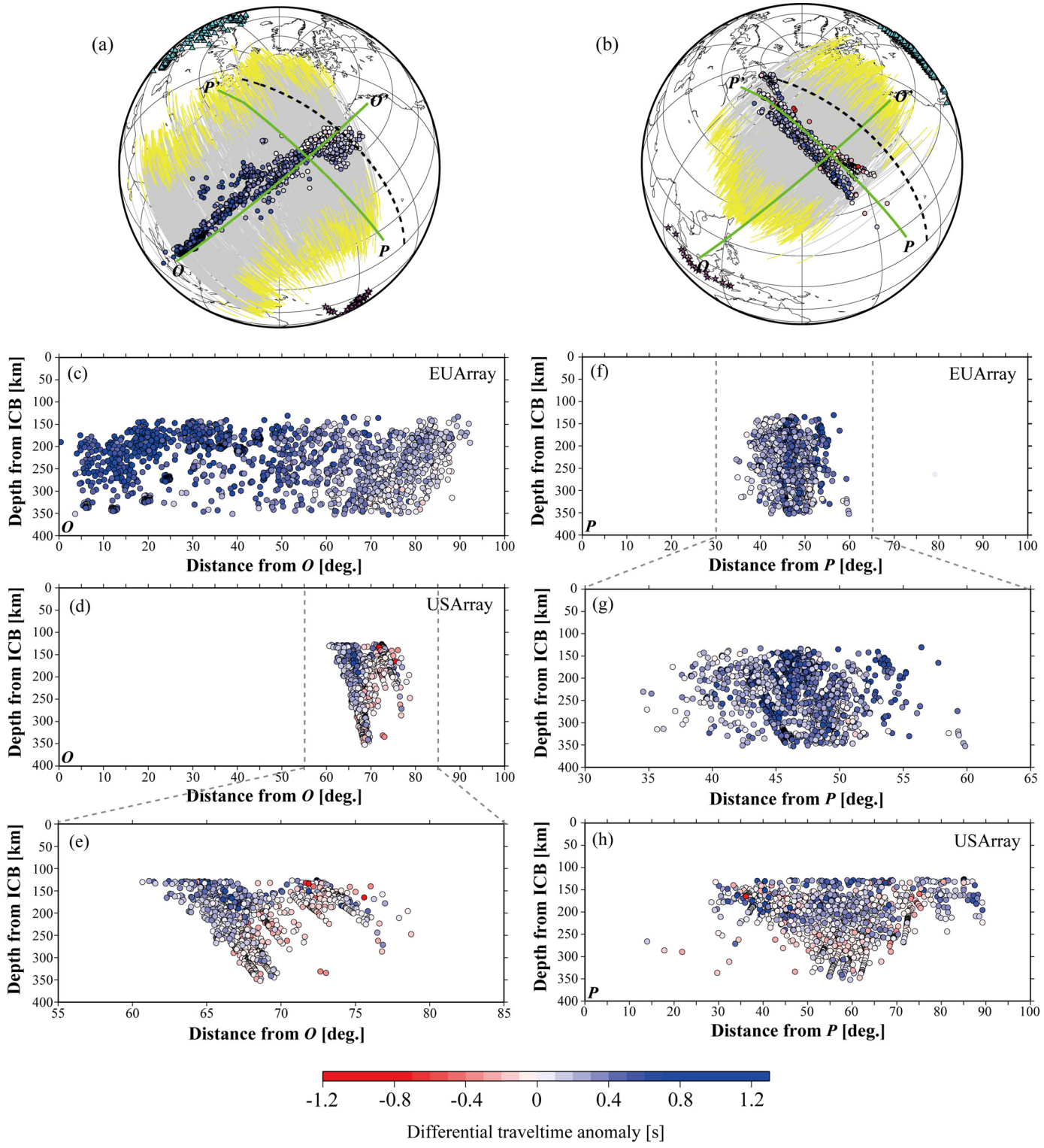

Fig. 4. The distribution of measured differential traveltime anomalies at the turning point of PKIKP: (a) a map-view for EUArray data, (b) a map-view for USArray data. Thin solid lines are ray paths of PKIKP in the inner core and ranges traveling in the top 100 km of the inner core are colored by yellow and ranges traveling in deeper than 100 km are colored by gray. The black dashed line denotes the hemispherical boundary obtained in this study. (c) A cross-section for EUArray data projected onto the great-circle plane from O to O' in (a) and (b). (d) A cross-section for USArray data similar to (c). (e) The same plot as (d) focused on the distance range from 55° to 85°. (f) A cross-section for EUArray data projected onto the great-circle plane from P to P' in (a) and (b). (g) The same plot as (f) focused on the distance range from 30° to 65°. (h) A cross-section for USArray data similar to (f).

boundary are counted. Note that this applies to about 60% of EUArray data and all for USArray data. Fig. 7b shows the variation of RMS residuals for variable boundary transition width. The error bars of RMS residuals are estimated by the bootstrap as done in a similar way in Section 3.2.

As a result, the minimum RMS residual is obtained at the width of ~600 km (28-degree angular distance), suggesting that a gradual transition over two hemispheres is better to explain observed differential traveltime anomalies rather than a sharp (step-like) boundary. The Fresnel zone of PKIKP with a dominant frequency

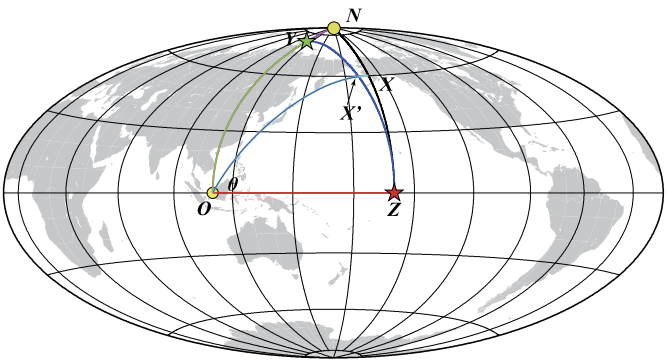

Fig. 5. The definition of the hemispherical boundary in this study. O is the origin of the coordinate at (0°N, 110°E) on the equator. N denotes the North Pole. Z and Y are variable points moving on the equator and on the meridian at 110°E. X and X' respectively denote points on the meridian at the longitude of Z and the defined boundary at an azimuth θ measured from the equator.

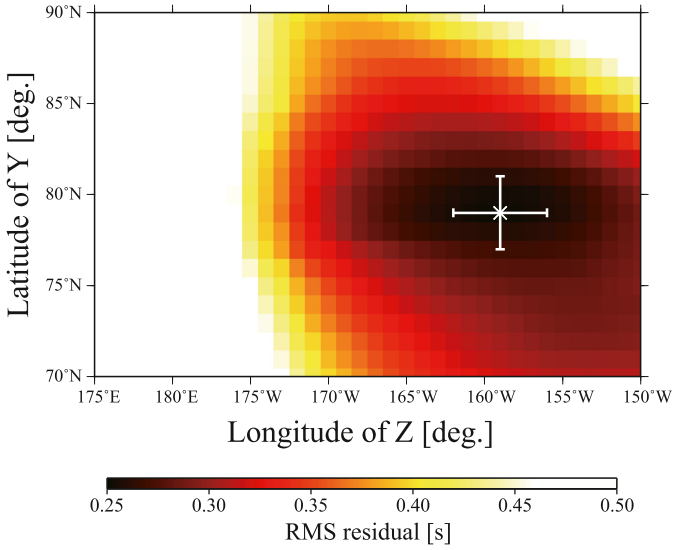

Fig. 6. RMS residuals between observed and calculated differential traveltime anomalies as functions of the longitude of Z and the latitude of Y shown in Fig. 4. The white cross symbol represents the minimum RMS point with error bars of Z and Y estimated by the bootstrap.

of 1 Hz is approximately ∼300 km wide (e.g. Calvet et al., 2006), and therefore, ∼600 km width of the velocity transition should be resolved. The RMS value reduction from 0 km width of transition to ∼600 km width is ∼0.022 s that is more than 10% of the RMS and significant. For the discussion of the transition width, we also compute residuals for boundaries corresponding to the end points of error bars in Fig. 6 (shown by the thinner lines in Fig. 7b). The variation depending on the latitude of Y shows larger RMS variation than that on the longitude of Z, and ±2° error of Y (Fig. 6) roughly corresponds to ±100 km of the width of the hemispherical transition. On the other hand, in terms of error bars of RMS for the best boundary cases (the red thick line in Fig. 7b), the error bar at 600 km width covers RMS values from 500 km width to 700 km width. From the results obtained in this analysis, we conclude that an arc-like boundary extending from 79°N, 110°E to 0°N, 159°W with 600 km width transition is the optimal hemispherical boundary model (hereafter referred to as the best transitional boundary model) and ±100 km uncertainty of width would be reasonable for the error estimates of boundary sharpness.

In Fig. 8, the best transitional boundary model is presented as a lateral velocity variation on the ICB (Fig. 8a) and as a depth section (Fig. 8b). The shape of the boundary is generally larger and more elongated along the equatorial direction than the circular boundary proposed by Tanaka and Hamaguchi (1997) (see Fig. 1b). As for the radial variation, the trajectory of the same velocity perturbation shifts with depth toward away from the boundary, i.e. toward the center of each hemisphere, as seen for 0.1% and 0.3% velocity perturbation lines in Fig. 8b. In Figs. 8c and 8e, the absolute value of the misfit between observations and theoretical traveltime anomalies for the best sharp boundary model, $|\Delta t_{\mathrm{obs}} - \Delta t_{\mathrm{cal}}(\mathrm{Sharp})|$, and for the best transitional boundary model, $|\Delta t_{\mathrm{obs}} - \Delta t_{\mathrm{cal}}(\mathrm{Transitional})|$, are plotted as a function of azimuth (measured from East; cf. Fig. 5), and averaged over a 10° azimuthal bin. It can be confirmed that, in both array data,

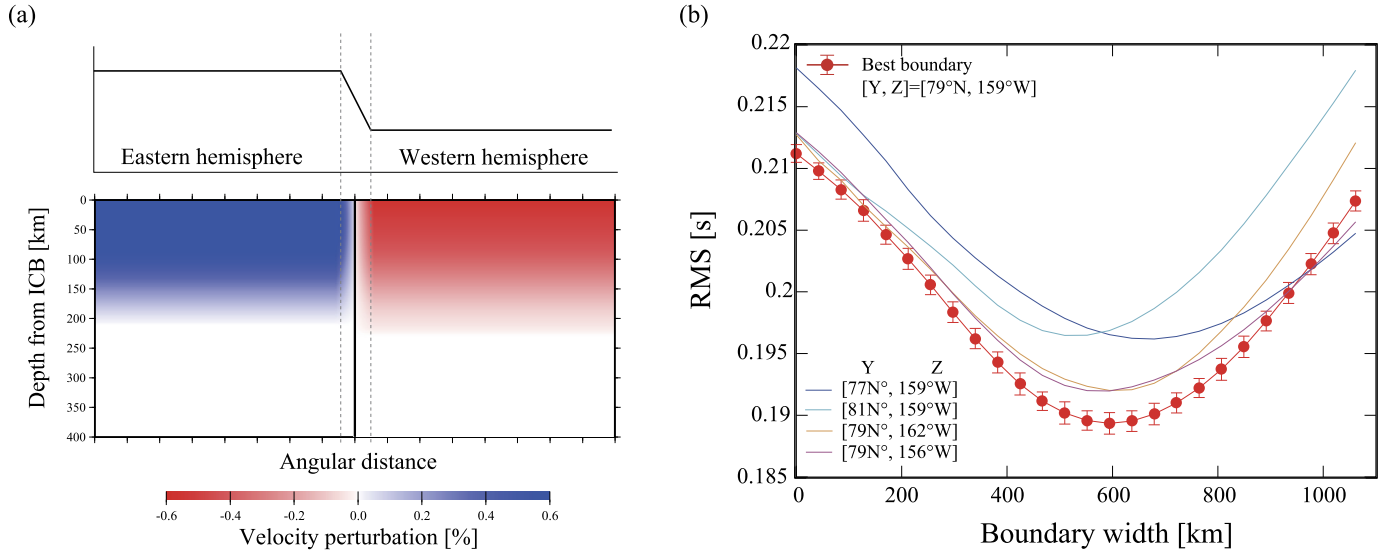

Fig. 7. (a) The definition of a linear transitional velocity structure. (top) The lateral variation of velocity perturbation at an arbitrary depth of the inner core. (bottom) A cross section of the velocity structure on the orthogonal plane to a hemispherical boundary. Gray dashed lines denote the width of the velocity transition. (b) The RMS residuals as a function of the transition width. Red plots with error bars represent the best boundary obtained in Section 3.2. Thinner lines are for boundaries defined by maximum and minimum points of the error bars for Y and Z shown in Fig. 5; [Y latitude, Z longitude] = [77°N, 159°W] (blue), [81°N, 159°W] (cyan), [79°N, 162°W] (orange), [79°N, 156°W] (magenta).

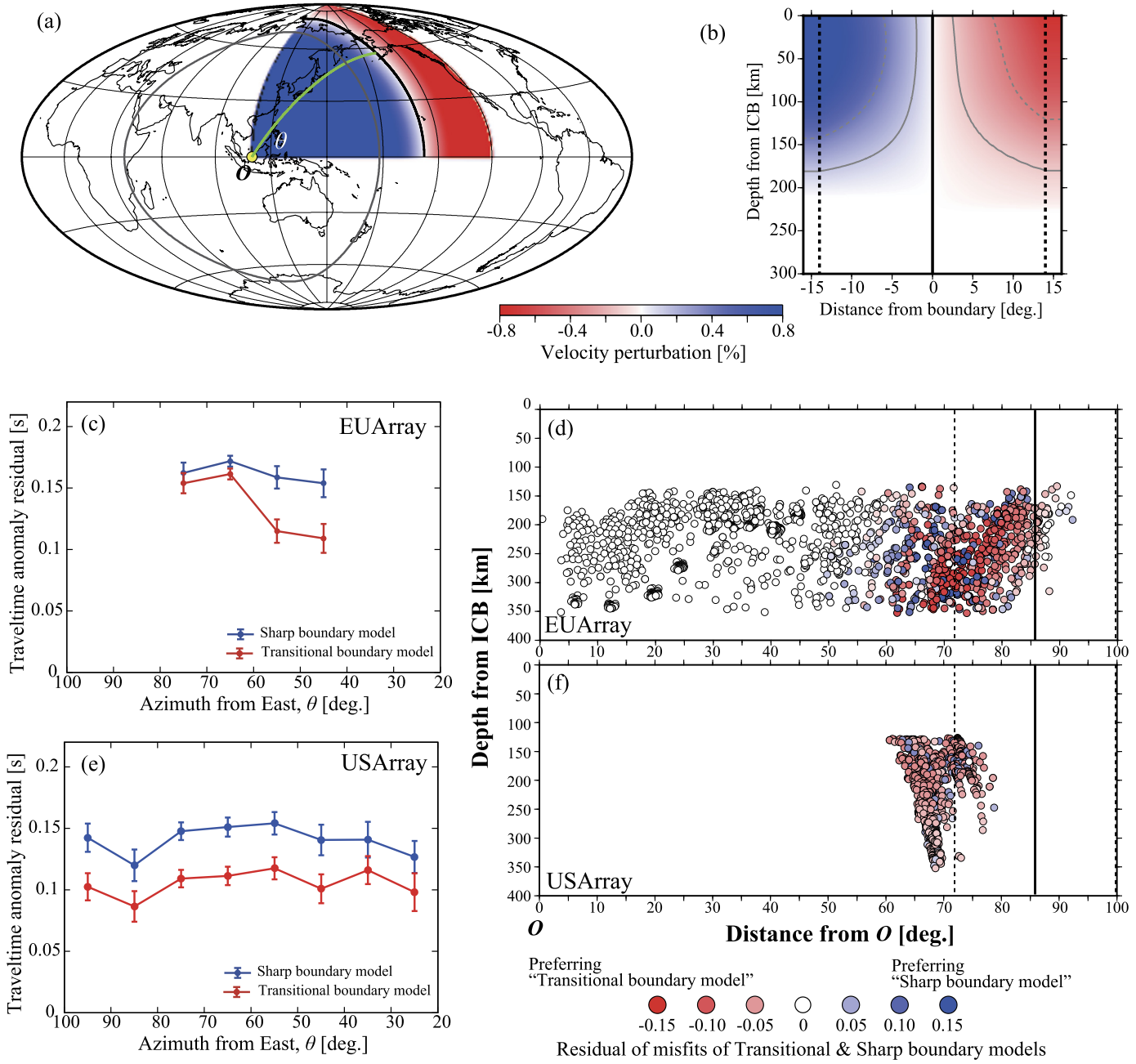

Fig. 8. (a) The lateral velocity perturbation of the proposed model at the ICB. The black line is the best boundary obtained in this study. (b) The cross-section of the velocity perturbation on a plane orthogonal to the best boundary, as a function of the angular distance from the boundary (the black solid line). The black dashed lines correspond to the width of the velocity transition. The gray solid and dashed lines represent contours at ±0.1% and ±0.3% of velocity perturbations. The color bar below (a) and (b) is common for both figures. (c) Azimuthal variation of the residuals of differential traveltime anomalies is compared for the best sharp boundary (blue) and the best transitional boundary (red) for EUArray data. Averages of absolute residuals for an azimuth bin of 10° are plotted. (d) The cross-section of the difference of misfits of two best boundary models at turning depths of PKIKP for EUArray data. The cross-section plane is shown by the green line (same as O–O' in Fig. 4a, b) in (a). The black solid and dashed lines indicate the best boundary and the transitional velocity width. Note that the cross-section plane is the same as in Figs. 4c–4e, and red (blue) color denotes the preference of the transitional (sharp) boundary model. (e) The same figure as (c) for USArray data. (f) The same figure as (d) for USArray data.

the best transitional boundary model shows smaller misfit than the best sharp boundary and no systematic bias is seen except for the azimuth range of 60°–80° in EUArray (Fig. 8c) where most of the rays propagate mainly in the eastern hemisphere of the inner core and are not affected by the boundary. Figs. 8d and 8f represent cross-sections of the difference of misfits of two boundary models, $|\Delta t_{\mathrm{obs}} - \Delta t_{\mathrm{cal}}(\mathrm{Transitional})| - |\Delta t_{\mathrm{obs}} - \Delta t_{\mathrm{cal}}(\mathrm{Sharp})|$, at the turning point of PKIKP ray paths onto a great-circle plane shown by the green line in Fig. 8a (and O–O' in Fig. 4a, b). In this definition of misfits, red (blue) color plots in Figs. 8d and 8f represent the preference of the best transitional (sharp) boundary model. The population of the negative value (red) is much higher than the positive value (blue), and this indicates that the best transitional boundary model better explains the observations in the region near the boundary. Note that, with the assumption of the linear transition, the differential traveltime anomaly has a substantial sensitivity to the shallow ($<\sim$100 km) structure as there is a larger velocity contrast in the shallow depths between the two hemispheres' models (Fig. 3e) and the analyzed shallow ray-paths cover significant portions of two hemispheres (Fig. 4a, b).

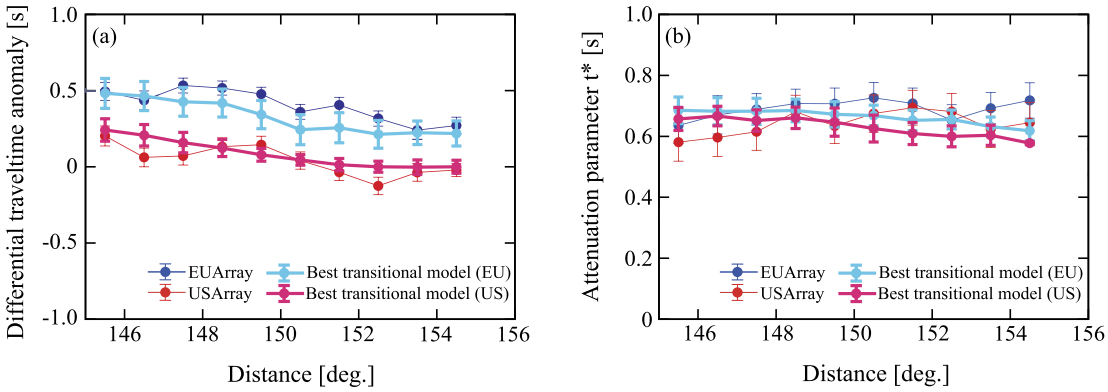

Fig. 9. Comparison of observed and model values for the differential traveltime anomaly (a) and the attenuation parameter (b). Blue and red plots with thin lines denote observed values for EUArray and USArray (the same plot in Fig. 3a, b), and cyan and magenta plots with thick lines represent model values. Averaged values for a distance bin of 1° are plotted.

Fig. 9 shows the comparison of observations and model values with the best transitional boundary model for the differential traveltime anomalies (Fig. 9a) and the attenuation parameters (Fig. 9b). Note that the attenuation parameter is computed by a similar way for the differential traveltime anomaly (equation (2)) as follows,

$$t^*_{\mathrm{cal}} = \int \frac{s_{\mathrm{east}}}{Q_{\mathrm{east}}} dl + \int \frac{s_{\mathrm{west}}}{Q_{\mathrm{west}}} dl \tag{4}$$

where $s_{\mathrm{east(west)}}$ and $Q_{\mathrm{east(west)}}$ are slowness and attenuation structures of Iritani et al. (2014a) (Figs. 3e and 3f). As for the attenuation structure, the sampling region of analyzed ray paths in the western hemisphere is corresponding to WH2 in the definition by Iritani et al. (2014a). Therefore, in the computation of theoretical attenuation parameters, we used the attenuation structure of WH2 in Iritani et al. (2014a) (the orange line in Fig. 3f). Moreover, attenuation structures (i.e. the values of Q^{-1}) are linearly connected over two hemispheres. Both parameters averaged over a 1-degree bin show good agreement, and it is confirmed that our model explains not only the differential traveltime anomaly but also higher attenuation parameters observed in both arrays. High attenuation parameters observed in the USArray data, in spite of small differential traveltimes, can be understood as due to the existence of high attenuation zone in depths of 100–300 km from the ICB beneath the northern Pacific as seen in the attenuation structure of WH2 (Fig. 3f). Such an attenuation structure was first reported by Kazama et al. (2008) and also resolved by Iritani et al. (2014a) and Attanayake et al. (2014). The attenuation parameter observation here further supports the presence of the high attenuation zone in the inner core beneath the eastern Pacific.

4. Discussion

4.1. Alternative causes for the differential traveltime anomaly?

The observed differential traveltime anomaly between PKIKP and PKPbc that we attributed to the hemispherical boundary might also be due to other causes, such as anisotropy of the inner core and/or the heterogeneities of the lowermost mantle. As for the anisotropic effect among two array data, we evaluate traveltime anomalies for PKIKP phase for the anisotropic velocity model of Irving and Deuss (2011) (0.5% and 4.8% anisotropy for the eastern and western hemisphere respectively). The difference of the traveltime anomaly between EUArray data (the angle range of ray paths from the Earth's rotation axis: 40°–60°) and USArray data (the angle range of ray paths from the Earth's rotation axis: 65°–75°) due to inner core anisotropy is ∼0.05 s that is nearly one order magnitude smaller than observed traveltime anomaly (∼0.3 s), and therefore the effect of anisotropy can be ignored.

As for the contribution of the heterogeneities at the lowermost mantle, the presence of a possible meso-scale ultralow-velocity-zone (ULVZ) at the core-mantle boundary (CMB) beneath the south Pacific (e.g. Yu and Garnero, 2018) might affect our observation of EUArray data. Considering that the separation distance between the incident points of PKIKP and PKPbc phases at the CMB is around 100 km (∼1.6 degree) and that the differential traveltime sees the effect only when two points are mutually on the opposite sides of the edge of the ULVZ (e.g. Long et al., 2018), we would expect to observe such an effect only for ray paths that go through near the edge within short distances (∼50 km or 0.8 degree) resulting in rather linear anomalies. The long wave-length (∼30 degree) differential traveltime anomaly variation as observed in Fig. 4c, the cause of which we attributed to the structure inside the inner core, therefore seems unlikely to be originated from the meso-scale ULVZ. Based on these considerations, we conclude that the observed differential traveltime anomaly mainly reflects the nature of the hemispherical heterogeneities of the inner core.

4.2. Comparisons with previous seismic studies

As we analyzed PKIKP and PKPbc, which are sensitive to the inner core structure in the top 350 km depth range, the best transitional boundary model has sufficient resolution in this depth range, and shows some agreements with previous studies that estimated the hemispherical boundary in the same inner core region. Miller et al. (2013) analyzed waveforms for events in the Philippines observed in South America whose ray paths are similar to USArray data of this study and estimated a boundary around a longitude of 173°E in a latitude range of 60°N–80°N in the uppermost 200 km of the inner core. Our model regionally matches with this result: the boundary we estimated locates at around 173°E at 72°N. On the other hand, Yu et al. (2017) analyzed PKIKP and PKPbc for events in subduction zones of the southwest Pacific observed in Europe whose ray paths are similar to EUArray data of this study, and their observation indicated a boundary at a longitude of 160°W. This result is in good agreement with our model around the equator. These comparisons suggest that our model is considered as a comprehensive model for these array data sets with different directions of ray paths. Ohtaki et al. (2012) observed a western-hemisphere-like slow velocity structure beneath Antarctica, indicating a similar arc-like hemispherical structure if assuming a symmetrical distribution in the southern hemisphere of the inner core. In the global scale, our arc-like model is qualitatively consistent with the harmonic (circular) boundary proposed

by Tanaka and Hamaguchi (1997), although it is equatorially elongated.

As for the depth variation of the velocity structure, our result suggests that hemispherical heterogeneities disappear around a depth of 200 km from the ICB (Fig. 8b), and this feature is consistent with the result of Miller et al. (2013). In previous seismic studies, however, it is suggested that hemispherical heterogeneities possibly exist in deeper parts of the inner core by analyses of body waves (Irving and Deuss, 2011; Tanaka, 2012) and normal modes (Deuss et al., 2010). Although the velocity depth profile of the inner core may still need further refinement, in Iritani et al. (2014a), we investigated the velocity structure of the top 350 km of the inner core by the waveform inversion analysis for globally collected array data and observed hemispherical heterogeneities only in the uppermost 200 km of the inner core. We, therefore, regard that velocity structures obtained by Iritani et al. (2014a) are reasonable to employ in this study, and the result of the analysis here further indicates that such modeling with heterogeneities in the top 200 km is sufficient to explain the observation presented in this study.

Irving and Deuss (2015) analyzed the differential traveltime between PKIKP and PKPbc for ray paths from the Kermadec-Tonga region to Europe, which are similar to those in this study (note that sampling coverage from 180°W–130°W in longitude) and from the Kuril-Kamchatka region to stations in Europe and South America, which sample east of our studied region. Although similar weak positive anomalies are measured in the overlapping sampling region for data observed in Europe (180°W–150°W longitude range) and westward shifting hemispherical boundary with increase of latitude is observed, their boundary locates at about 10° eastern side relative to the transitional edge of our model for their result of the isotropic velocity. This inconsistency could be caused by two factors: (1) they modeled the velocity structures by patches with 30° longitude range and therefore the boundary resolution would be limited by this longitude interval; (2) the high positive anomalies observed in ray paths from Kuril to South America sampling in the longitude range of 150°W–130°W. Moreover, they estimated the anisotropic velocity structure and obtained anisotropic feature in the eastern hemisphere with highest anisotropy in 150°W–130°W longitude range and no anisotropy in the western hemisphere which is opposite from the knowledge suggested by previous studies. Although the analyzed data used in our study have no sensitivity for the anisotropy as mentioned in Section 3.1, this complex anisotropic feature may be related to the transitional hemispherical structure we observed.

Also, our result gives qualitative interpretations for previous seismic observations for the shallower part of the inner core. Ibourichene and Romanowicz (2018) observed slower velocity than AK135 in the top 100 km of the northern part of the eastern hemisphere by processing similar ray paths used in this study, from events near Sumatra to USArray. This observation favors an arc-like hemispherical boundary as obtained in this study, rather than a meridian boundary. In the radial variation of hemispherical structure, Waszek et al. (2011) measured differential traveltime between PKIKP and PKiKP for globally collected data and observed the eastward depth shift of the boundary. Focusing on the radial variation of the negative velocity perturbation shown in Fig. 8b, contours of the same velocity perturbation value vary eastward with depth. Assuming such variation of the velocity perturbation as a hemispherical boundary, the depth-shifting boundary might be explained by the transitional velocity structure. Moreover, in their differential traveltime anomaly measurements, negative anomalies are observed at higher latitude than 30°N even in the eastern hemisphere in a depth range of 57.5–106 km (Fig. S1 in Waszek et al., 2011), indicating a similar arc-like feature with our model.

4.3. Geodynamical implications

According to the inner core growth modeling affected by thermochemical flows in the outer core coupled with thermal heterogeneities at the CMB (Sumita and Olson, 1999; Aubert et al., 2008; Gubbins et al., 2011), the heterogeneities of the inner core structure are characterized by the different growth rate of iron, and the distribution of growth rates shows larger variation from the fastest growth rate region beneath south-east Asia to the Polar direction than to the equatorial direction; i.e., the area with the faster growth rate relative to the average, corresponding to a faster velocity structure, elongates equatorially from the fastest growth rate region, and the growth rate becomes around the average value at the central part of the Pacific, while slower growth rate areas (i.e., a slower velocity) are distributed beneath the Polar regions. With this model, the obtained arc-like boundary that is equatorially elongated is qualitatively explained, although it is still unclear how the sharpness of the hemispherical boundary developed by thermal heterogeneities of CMB.

Alternatively, our transitional boundary model shows more consistencies with the translational grain growth model of iron proposed by Monnereau et al., 2010 and Alboussière et al., 2010. Geballe et al. (2013) numerically simulated differential traveltime residuals of PKIKP – PKiKP for global data by considering the translational grain growth model, and compared with seismic observations by Waszek and Deuss (2011). They argued that only the cubic iron crystal (*bcc*) with high anisotropic elasticity (Belonoshko et al., 2007) was able to explain the magnitude and the rapid hemispherical variation of differential traveltime anomalies observed in Waszek and Deuss (2011). In their simulation, however, theoretical differential traveltime residuals gradually shift from negative to positive values in a ∼30-degree angular distance range due to the continuous translation of iron with grain growth (Fig. 3 of Geballe et al., 2013). This transition range shows a good agreement with the sharpness estimated in this study, ∼28-degree angular distance. More recently, Lasbleis et al. (2017) simulated fast and slow translational models with and without extremely slow superrotation of the inner core (Aubert and Dumberry, 2011). Assuming the hemispherical boundary as the contour of the same iron crystal age, the boundary gradually shifts with depth toward the center of each hemisphere (Fig. 3 of Lasbleis et al., 2017). This feature is qualitatively consistent with the depth variation of velocity perturbations shown in Fig. 8b of this study.

Although the translational growth model is capable of explaining the hemispherical heterogeneities of isotropic velocity and attenuation and the transitional boundary model observed here, there are still several concerns to fully accept this model as the cause of the hemispherical heterogeneity. One is that this model does not explain other seismic observations, such as the presence of rotation-axial anisotropy (e.g. Creager, 1992; Garcia and Souriau, 2000; Irving and Deuss, 2011), and the existence of the innermost inner core (e.g. Ishii and Dziewonski, 2002). Another concern is that, for the degree-one translational convection to occur, a viscosity greater than the order of 10^{18} Pa s is required, and under such a lower viscosity condition, large-scale plume convection becomes dominant (Deguen and Cardin, 2011; Deguen et al., 2013). The viscosity of the inner core is previously estimated in the range of 10^{11}–10^{22} Pa s (e.g. Yoshida et al., 1996; Buffett, 1997; Koot and Dumberry, 2011), and therefore, both scenarios are acceptable with the present estimates of the inner core viscosity.

In addition to these viscosity uncertainties, a lower shear velocity than previously thought is estimated by the recent seismic

observation of PKJKP phase, that shear wave propagating in the inner core (Tkalčić and Pham, 2018), and this observation might indicate a soft inner core. Therefore, as an alternative interpretation of our result, a hypothesis of a large-scale plume convection under a low viscosity condition might be plausible (e.g. Deguen et al., 2013): with this scenario, the velocity transition in our result is considered as due to an up-welling (or down-welling) convective plume, and the gradual variation of velocity structure would be achieved if the temperature difference between two hemispheres is extremely small (an order of milli-Kelvins is estimated by Buffet, 1997).

5. Conclusion

We investigated the hemispherical boundary and its transition width of the inner core beneath the northern Pacific. Nearly 3,300 waveforms comprising two directional event-array pairs are analyzed via the nonlinear waveform inversion method to measure the traveltime and the attenuation parameter of core phases. Our measurements of the differential traveltime anomaly between PKIKP and PKPbc indicate that the arc-like-shaped hemispherical boundary, which is located at (0°N, 159°W) on the equator and (79°N, 110°E) at the northernmost point with a ∼600km-wide velocity transition, is more suitable than a meridian and/or sharp (step-like) boundary. This transitional boundary model can comprehensively account for the observations made previously estimated in the studied region. Although our finding of the transitional boundary appears generally consistent with the convective translational grain growth model, it may not be the unique interpretation.

Acknowledgements

Waveforms analyzed in this study are collected from the Data Management Center of Incorporated Research Institutions for Seismology (IRIS DMC). We acknowledge Dr. H. Shimizu and Dr. S. Tanaka for helpful discussions and comments on the manuscript. We also thank two anonymous reviewers for their constructive comments that improved the clarity of the manuscript. We use the Generic Mapping Tools (Wessel and Smith, 1998) for drawing some of the figures, and the Taup software (Crotwell et al., 1999) for the calculation of traveltimes. This research is partly supported by JSPS KAKENHI Grant Number JP15H05832.

References

Alboussière, T., Deguen, R., Melzani, M., 2010. Melting-induced stratification above the Earth's inner core due to convective translation. Nature 466, 744–747.
Attanayake, J., Cormier, V.F., de Silva, S.M., 2014. Uppermost inner core seismic structure – new insights from body waveform inversion. Earth Planet. Sci. Lett. 385, 49–58.
Aubert, J., Amit, H., Hulot, G., Olson, P., 2008. Thermochemical flows couple the Earth's inner core growth to mantle heterogeneity. Nature 454, 758–761.
Aubert, J., Dumberry, M., 2011. Steady and fluctuating inner core rotation in numerical geodynamo models. Geophys. J. Int. 184, 162–170.
Belonoshko, A., Skorodumova, N., Davis, S., Osiptsov, A., Rosengren, A., Johansson, B., 2007. Origin of the low rigidity of the Earth's inner core. Science 316, 1603–1605.
Buffett, B.A., 1997. Geodynamics estimates of the viscosity of the Earth's inner core. Nature 388, 571–573.
Calvet, M., Chevrot, S., Souriau, A., 2006. P-wave propagation in transversely isotropic media: II. Application to inner core anisotropy: effects of data averaging, parameterization and a priori information. Phys. Earth Planet. Inter. 156, 21–40.
Cao, A., Romanowicz, B., 2004. Hemispherical transition of seismic attenuation at the top of the Earth's inner core. Earth Planet. Sci. Lett. 228, 243–253.
Cormier, V.F., Attanayake, J., 2013. Earth's solid inner core: seismic implications of freezing and melting. J. Earth Sci. 24, 683–698.
Creager, K.C., 1992. Anisotropy of the inner core from differential travel times of the phases PKP and PKIKP. Nature 356, 309–314.
Crotwell, H.P., Owens, T.J., Ritsema, J., 1999. The TauP toolkit: flexible seismic traveltime and ray-path utilities. Seismol. Res. Lett. 70, 154–160.
Deguen, R., 2012. Structure and dynamics of Earth's inner core. Earth Planet. Sci. Lett. 333–334, 211–225.
Deguen, R., Alboussière, T., Cardin, P., 2013. Thermal convection in Earth's inner core with phase change at its boundary. Geophys. J. Int. 194 (3), 1310–1334.
Deguen, R., Cardin, P., 2011. Thermochemical convection in Earth's inner core. Geophys. J. Int. 187 (3), 1101–1118.
Deuss, A., Irving, J., Woodhouse, J., 2010. Regional variation of inner core anisotropy from seismic normal mode observations. Science 328, 1018–1020.
Efron, B., Tibshirani, R.J., 1993. An Introduction to the Bootstrap. Monographs on Statistics and Applied Probability, vol. 57. Chapmann & Hall.
Garcia, R., Souriau, A., 2000. Inner core anisotropy and heterogeneity level. Geophys. Res. Lett. 27 (19), 3121–3124.
Garcia, R., 2002. Constrains on upper inner-core structure from waveform inversion of core phases. Geophys. J. Int. 150 (3), 651–664.
Garcia, R., Chevrot, S., Weber, M., 2004. Nonlinear waveform and delay time analysis of triplicated core phases. J. Geophys. Res. 109, B01306.
Geballe, Z.M., Lasbleis, M., Cormier, V.F., Day, E.A., 2013. Sharp hemisphere boundaries in a translating inner core. Geophys. Res. Lett. 40 (9), 1719–1723.
Gubbins, D., Sreenivasan, B., Mound, J., Rost, S., 2011. Melting of the Earth's inner core. Nature 473, 361–363.
Ibourichene, A., Romanowicz, B., 2018. Detection of small scale heterogeneities at the inner core boundary. Phys. Earth Planet. Inter. 281, 55–67.
Iritani, R., Takeuchi, N., Kawakatsu, H., 2010. Seismic attenuation structure of the top half of the inner core beneath the northeastern Pacific. Geophys. Res. Lett. 37, L19303.
Iritani, R., Takeuchi, N., Kawakatsu, H., 2014a. Intricate heterogeneous structures of the top 300 km of the Earth's inner core inferred from global array data: I. Regional 1D attenuation and velocity profiles. Phys. Earth Planet. Inter. 230, 15–27.
Iritani, R., Takeuchi, N., Kawakatsu, H., 2014b. Intricate heterogeneous structures of the top 300 km of the Earth's inner core inferred from global array data: II. Frequency dependence of inner core attenuation and its implication. Earth Planet. Sci. Lett. 405, 231–243.
Irving, J.C.E., Deuss, A., 2011. Hemispherical structure in inner core velocity anisotropy. J. Geophys. Res. 116 (B4), B04307.
Irving, J.C.E., Deuss, A., 2015. Regional seismic variations in the inner core under the North Pacific. Geophys. J. Int. 203 (3), 2189–2199.
Ishii, M., Dziewonski, A., 2002. The innermost inner core of the Earth: evidence for a change in anisotropic behavior at a radius of about 300 km. Proc. Natl. Acad. Sci. USA 99, 14026–14030.
Kazama, T., Kawakatsu, H., Takeuchi, N., 2008. Depth-dependent attenuation structure of the inner core inferred from short-period Hi-net data. Phys. Earth Planet. Inter. 167, 155–160.
Kennett, B.L.N., Engdahl, E.R., Buland, R., 1995. Constraints on seismic velocities in the Earth from traveltimes. Geophys. J. Int. 122, 108–124.
Koot, L., Dumberry, M., 2011. Viscosity of the Earth's inner core: constraints from nutation observations. Earth Planet. Sci. Lett. 308, 343–349.
Lasbleis, M., Waszek, L., Day, E.A., 2017. GrowYourIC: a step toward a coherent model of the Earth's inner core seismic structure. Geochem. Geophys. Geosyst. 18, 4016–4026.
Long, X., Kawakatsu, H., Takeuchi, N., 2018. A sharp structural boundary in lowermost mantle beneath Alaska detected by core phase differential travel times for the anomalous South Sandwich Islands to Alaska path. Geophys. Res. Lett. 45 (1), 176–184.
Miller, M.S., Niu, F., Vanacore, E.A., 2013. Aspherical structural heterogeneity within the uppermost inner core: insights into the hemispherical boundaries and core formation. Phys. Earth Planet. Inter. 223, 8–20.
Mizzon, H., Monnereau, M., 2013. Implication of the lopsided growth for the viscosity of Earth's inner core. Earth Planet. Sci. Lett. 361, 391–401.
Monnereau, M., Calvet, M., Margerin, L., Souriau, A., 2010. Lopsided growth of Earth's inner core. Science 328, 1014–1017.
Ohtaki, T., Kaneshima, S., Kanjo, K., 2012. Seismic structure near the inner core boundary in the south polar region. J. Geophys. Res. 117, B03312.
Pejić, T., Hawkins, R., Sambridge, M., Tkalčić, H., 2019. Transdimensional Bayesian attenuation tomography of the upper inner core. J. Geophys. Res., Solid Earth 124.
Sen, M., Stoffa, P., 1995. Global Optimization Methods in Geophysical Inversion. Elsevier Sci., New York.
Sumita, I., Olson, P., 1999. A laboratory model for convection in Earth's core driven by a thermally heterogeneous mantle. Science 286 (5444), 1547–1549.
Tanaka, S., Hamaguchi, H., 1997. Degree one heterogeneity and hemispherical variation of anisotropy in the inner core from PKP(BC)-PKP(DF) times. J. Geophys. Res. 102, 2925–2938.
Tanaka, S., 2012. Depth extent of hemispherical inner core from PKP(DF) and PKP(Cdiff) for equatorial paths. Phys. Earth Planet. Inter. 210–211, 50–62.
Tkalčić, H., Phạm, T.-S., 2018. Shear properties of Earth's inner core constrained by a detection of J waves in global correlation wavefield. Science 362 (6412), 329–332.
Waszek, L., Deuss, A., 2011. Distinct layering in the hemispherical seismic velocity structure of Earth's upper inner core. J. Geophys. Res. 116 (B12), B12313.

Waszek, L., Irving, J.C.E., Deuss, A., 2011. Reconciling the hemispherical structure of Earth's inner core with its super-rotation. Nat. Geosci. 4 (4), 264–267.
Wen, L., Niu, F., 2002. Seismic velocity and attenuation structures in the top of the Earth's inner core. J. Geophys. Res. 107 (B11), 2273.
Wessel, P., Smith, H.W.F., 1998. New, improved version of the Generic Mapping Tools released. Eos Trans. AGU 79, 579.
Yoshida, S.I., Sumita, I., Kumazawa, M., 1996. Growth model of the inner core coupled with the outer core dynamics and the resulting elastic anisotropy. J. Geophys. Res. 101, 28085.
Yu, S., Garnero, E.J., 2018. Ultralow velocity zone locations: a global assessment. Geochem. Geophys. Geosyst. 19, 396–414.
Yu, W., Wen, L., 2006. Seismic velocity and attenuation structures in the top 400 km of the Earth's inner core along equatorial paths. J. Geophys. Res. 111, B07308.
Yu, W., Su, J., Song, T., Huang, H., Mozziconacci, L., Huang, B., 2017. The inner core hemispheric boundary near 180°W. Phys. Earth Planet. Inter. 272, 1–16.